

Testing wave turbulence theory for Gross-Pitaevskii system

Ying Zhu,^{1,*} Boris Semisalov,^{2,3,4} Giorgio Krstulovic,² and Sergey Nazarenko¹

¹*Université Côte d'Azur, CNRS, Institut de Physique de Nice - INPHYNI, Parc Valrose, 06108 Nice, France*

²*Université Côte d'Azur, Observatoire de la Côte d'Azur, CNRS, Laboratoire Lagrange, Boulevard de l'Observatoire CS 34229 - F 06304 Nice Cedex 4, France*

³*Novosibirsk State University, 1 Pirogova street, 630090 Novosibirsk, Russia*

⁴*Sobolev Institute of Mathematics SB RAS, 4 Academician Koptyug Avenue, 630090 Novosibirsk, Russia*

We test the predictions of the theory of weak wave turbulence by performing numerical simulations of the Gross-Pitaevskii equation (GPE) and the associated wave-kinetic equation (WKE). We consider an initial state localized in Fourier space, and we confront the solutions of the WKE obtained numerically with GPE data for both, the waveaction spectrum and the probability density functions (PDFs) of the Fourier mode intensities. We find that the temporal evolution of GP data is accurately predicted by the WKE, with no adjustable parameters, for about two nonlinear kinetic times. Qualitative agreement between the GPE and the WKE persists also for longer times with some quantitative deviations that may be attributed to the breakdown of the theoretical assumptions underlying the WKE. Furthermore, we study how the wave statistics evolves toward Gaussianity in a time scale of the order of the kinetic time. The excellent agreement between direct numerical simulations of the GPE and the WKE provides a new and solid ground to the theory of weak wave turbulence.

I. INTRODUCTION

Wave Turbulence (WT) is a state of continuous medium characterized by presence of random mutually interacting waves with a broadband spectrum. Weak WT theory (WWT) is a mathematical framework describing the statistical behavior of WT dominated by weakly nonlinear waves. The main object in this theory is the waveaction spectrum which is the second-order moment of the wave amplitude and which evolves according to the so-called wave-kinetic equation (WKE). Special attention in past literature was given to studies of stationary scaling solutions of this equation which are analogous to the Kolmogorov spectrum of hydrodynamic turbulence, the so-called Kolmogorov-Zakharov (KZ) spectra. However, nonstationary WT is also interesting because it is often characterized by mathematically nontrivial solutions exhibiting self-similar asymptotic [1–6]. Moreover, WWT can be also extended to describing the higher-order moments and even to the full joint probability density function (PDF) of the wave intensities [7–11]. An introduction to WT as well as a summary of recent developments in this area can be found in book [7]. Some fundamental concepts of WT were laid out in an older text [12]. Recent book [13] contains a collection of reviews about recent experiments in WT.

Over the past few years, a significant push was made in the direction of rigorous mathematical justification of the WWT. The state of the art result is a claim made in [14] that the WKE (9) derived from the 3D Gross-Pitaevskii equation (GPE) (1) truthfully predicts evolution of the wave spectrum (under certain requirements on the initial conditions) up to a time $\delta \cdot T_{kin}$ where T_{kin} is the

characteristic evolution time of the WKE and $\delta \ll 1$. This result is significant from the mathematical point of view because δ is independent of the (vanishing) nonlinearity strength and the (expanding to infinity) physical size of the system. As such this result is the wave analog of the famous Lanford's theorem on the Boltzmann kinetic equation from colliding particle systems. However, this result is insufficient for physical applications, in the majority of which one is interested in evolution at times $\gtrsim T_{kin}$ when the spectrum has significantly evolved away from its initial shape, whereas at time $\delta \cdot T_{kin}$ it is still very close to the initial one.

Thus, the main motivation of the present study is to test WWT at the times $\gtrsim T_{kin}$ by juxtaposition of the spectra arising from the direct numerical simulations (DNS) of the 3D GPE (1) and from the simulations of the WKE (9). Further, for the first time we explore numerically the evolution of the wave-intensity PDFs and the statistical quantities associated with it, e.g. the cumulants. We show that both the spectra and the PDFs for the WKE and the GPE agree with each other very well for times $\gtrsim T_{kin}$, and we characterize the departures at later times.

Note that a similar in spirit comparison of the evolving spectra arising in the numerics of WKE and the original dynamic model was done in [15] for the deep water surface gravity waves. Their study was oriented on the practical problem of the sea swell modeling, with comparisons made on a qualitative level of visual comparing the plots. Further modifications by introducing dissipation and forcing were explored with a view to make the models more realistic for practical modeling of the sea waves. In contrast, our study is aimed at the more fundamental aspects of the WWT validity rather than a particular real life wave phenomenon. In order to make the comparisons be like-for-like, we do not introduce any extra terms to improve the modeling. We introduce global

* yzhu@unice.fr

measures characterizing the spectra, such as the energy and the waveaction centroids, to make our comparisons more quantitative.

The present paper is organized as follows. In Section II we introduce the GPE and the setting we consider in this work. We provide then a short introduction to the theory of weak wave turbulence and present the wave-kinetic equation. The dynamics of the probability distribution functions of the wave-action spectra is also discussed. In Section III, we explain our numerical methods for integrating the GPE and the WKE. Then, in Section IV we present our numerical results where we directly compare numerical simulations of the GPE and the WKE. Finally, in Section V we present our conclusions. We took out the details on derivation of the WKE in isotropic homogeneous setup to the Appendix A and discuss the most important issues of the new numerical algorithm used for solving WKE in Appendix B.

II. THEORETICAL BACKGROUND

A. Gross-Pitaevskii equation

The dimensionless Gross-Pitaevskii Equation (GPE) in a 3D physical space $\mathbf{r} = \{x, y, z\}$ for the complex wave function $\psi(\mathbf{r}, t)$ is

$$i \frac{\partial \psi(\mathbf{r}, t)}{\partial t} = \left[-\nabla^2 + |\psi(\mathbf{r}, t)|^2 \right] \psi(\mathbf{r}, t). \quad (1)$$

This equation describes dynamics of Bose-Einstein condensates (BEC) [16], nonlinear light [17] and other important physical systems, and as such it is a universal master equation that allows to study fundamental nonlinear phenomena including the nonlinear wave interactions. Consider the nonlinear wave system described by the GPE (1) in the L -periodic box of volume $V = L^3$. From GPE (1) we have the following Hamiltonian equations for the Fourier coefficients of the wave function,

$$i \dot{a}_{\mathbf{k}} = \frac{\partial \mathcal{H}}{\partial a_{\mathbf{k}}^*}, \quad (2)$$

$$\mathcal{H} = \sum_{\mathbf{k}} \omega_{\mathbf{k}} |a_{\mathbf{k}}|^2 + \frac{1}{2} \sum_{\mathbf{k}_1, \mathbf{k}_2, \mathbf{k}_3, \mathbf{k}_4} a_{\mathbf{k}_1}^* a_{\mathbf{k}_2}^* a_{\mathbf{k}_3} a_{\mathbf{k}_4} \delta_{12}^{34},$$

where $\mathbf{k}, \mathbf{k}_1, \mathbf{k}_2, \mathbf{k}_3, \mathbf{k}_4 \in \frac{L}{2\pi} \mathbb{Z}^3$ are the wave vectors, $\omega_{\mathbf{k}} = k^2$ is the frequency of mode \mathbf{k} , $k = |\mathbf{k}|$, and $a_{\mathbf{k}} \in \mathbb{C}$ is the waveaction variable:

$$a_{\mathbf{k}} = \hat{\psi}_{\mathbf{k}} = \frac{1}{V} \int \psi(\mathbf{r}, t) e^{-i\mathbf{k} \cdot \mathbf{r}} d\mathbf{r}, \quad (3)$$

$\delta_{12}^{34} = \delta(\mathbf{k}_1 + \mathbf{k}_2 - \mathbf{k}_3 - \mathbf{k}_4)$, and the integral is taken over all the possible discrete values of $\mathbf{k}_1, \mathbf{k}_2, \mathbf{k}_3$ and \mathbf{k}_4 .

The GPE (1) conserves the mean density of particles,

$$N = \frac{1}{V} \int |\psi(\mathbf{x}, t)|^2 d\mathbf{x} \quad (4)$$

and the mean density of energy,

$$H = \frac{1}{V} \int \left[|\nabla \psi(\mathbf{x}, t)|^2 + \frac{1}{2} |\psi(\mathbf{x}, t)|^4 \right] d\mathbf{x}. \quad (5)$$

The total energy density can be split into two parts – the energy density of the linear-dynamics $H_2 = \frac{1}{V} \int |\nabla \psi(\mathbf{x}, t)|^2 d\mathbf{x}$, and the nonlinear-dynamics energy $H_4 = \frac{1}{V} \int \frac{1}{2} |\psi(\mathbf{x}, t)|^4 d\mathbf{x}$. In a wave turbulent state, the total energy and the density of particles cascade in opposite directions.

An important quantity, which characterizes the system, is the healing length, $\xi = \frac{1}{\sqrt{N}}$, which refers to an average scale at which the nonlinear term becomes comparable with the linear one. The characteristic wave number corresponding to ξ is defined as $k_\xi = \frac{1}{\xi}$.

Also, we define the condensate fraction as

$$C_0 = \frac{|\hat{\psi}_0|^2}{N}. \quad (6)$$

$C_0 = 0$ means that there is no homogeneous condensate in the field, and $C_0 = 1$ represents a complete condensation. When the condensate fraction is small or absent, and the waves are weak, the system described by GPE can be modelled within the WWTT approach leading to the four-wave WKE [7] introduced in the next subsection.

B. Wave-kinetic equation description

The analysis of the GPE in the case of weak nonlinearity leads to the integro-differential WKE describing the evolution of the waveaction spectrum

$$n_{\mathbf{k}}(t) = n(\mathbf{k}, t) = \left(\frac{L}{2\pi} \right)^3 \langle |a_{\mathbf{k}}|^2 \rangle, \quad (7)$$

where the brackets denote averaging over the initial wave statistics.

To make all further considerations consistent with the WWTT, let us briefly summarise the basic steps of derivation of WKE from GPE [7]:

- Consider GPE in the Fourier space.
- Set a small parameter $\varepsilon > 0$, which is the measure of nonlinearity, and consider GPE on the intermediate time scale T_I between the linear and nonlinear time scales:

$$\frac{2\pi}{k^2} (\text{linear scale}) \ll T_I \sim \frac{2\pi}{\varepsilon k^2} \ll \frac{2\pi}{\varepsilon^2 k^2} (\text{nonlinear scale}).$$

- Introduce the interaction representation variable,

$$\hat{b}_{\mathbf{k}}(t) = \frac{1}{\sqrt{\varepsilon}} \hat{\psi}_{\mathbf{k}} \exp(i\tilde{\omega}_{\mathbf{k}} t), \quad \tilde{\omega}_{\mathbf{k}} = k^2 + 2N. \quad (8)$$

Here, the second term in $\tilde{\omega}_{\mathbf{k}}$ is the so-called nonlinear frequency shift: it is the leading order nonlinear

effect, but it does not lead to energy exchanges between the Fourier modes — hence one has to consider the next order.

- assume that *initially* the amplitudes $|\hat{b}_k|$ and the phase factors $\hat{b}_k/|\hat{b}_k|$ are statistically independent random variables, and the phase factors are uniformly distributed on the unit circle in the complex plane — this is the so-called Random Phase and Amplitude (RPA) property.

- Make the asymptotic expansion of $\hat{b}_k(T_I)$ with respect to the small parameter ε , substitute it into GPE and find the averaged coefficients with the aid of the RPA property.
- Approximate the time derivative of the waveaction spectrum by difference quotient, express it through the obtained averaged coefficients and pass first to the large box limit $L \rightarrow \infty$ (which makes the k -space continuous). Then pass to the limit $T_I \rightarrow \infty$.

As the result, one obtains the following WKE for the four-wave interaction $\mathbf{k}, \mathbf{k}_1 \rightarrow \mathbf{k}_2, \mathbf{k}_3$:

$$\frac{d}{dt}n_{\mathbf{k}} = 4\pi \int \delta(\mathbf{k} + \mathbf{k}_1 - \mathbf{k}_2 - \mathbf{k}_3)\delta(\omega_{\mathbf{k}} + \omega_{\mathbf{k}_1} - \omega_{\mathbf{k}_2} - \omega_{\mathbf{k}_3}) [n_{\mathbf{k}_1}n_{\mathbf{k}_2}n_{\mathbf{k}_3} + n_{\mathbf{k}}(n_{\mathbf{k}_2}n_{\mathbf{k}_3} - n_{\mathbf{k}_1}n_{\mathbf{k}_3} - n_{\mathbf{k}_1}n_{\mathbf{k}_2})] d\mathbf{k}_1 d\mathbf{k}_2 d\mathbf{k}_3, \quad (9)$$

where δ is the Dirac δ -function, and wavevectors are now continuous ($\mathbf{k}_i \in \mathbb{R}^3$).

The collision integral in the right-hand-side (RHS) of (9) is taken over a 9-dimensional space. However, we shall consider the situation when the wave fields are isotropic. In this situation, averaging over directions reduces considerably the dimension of integration. Such simplification gives the possibility to study complex non-stationary self-similar solutions of the second kind, see for instance [1–3, 6, 18]. Performing the angle averaging leads to a new collision kernel. Previous results presented in the literature reported disparate pre-factors of the kernel [1, 12, 19]. The value of this pre-factor is crucial for a quantitative comparison of the evolution of GPE and WKE solutions. In Appendix A we provide a careful derivation, where we have corrected previous errors.

Assuming the isotropy, we consider the waveaction spectrum that depends only on $k = |\mathbf{k}|$ and pass to the frequency variable: $n_{\mathbf{k}}(t) = n_{\omega}(t) = n(\omega, t)$, where $\omega = k^2$ is the new variable. The isotropic WKE is

$$\frac{d}{dt}n_{\omega} = \frac{4\pi^3}{\sqrt{\omega}} \int S(\omega, \omega_1, \omega_2, \omega_3)\delta_{1\omega}^{23} n_{\omega}n_1n_2n_3 \quad (10)$$

$$(n_{\omega}^{-1} + n_1^{-1} - n_2^{-1} - n_3^{-1}) d\omega_1 d\omega_2 d\omega_3.$$

where $\delta_{1\omega}^{23} = \delta(\omega + \omega_1 - \omega_2 - \omega_3)$. The integral in the RHS of (10) is taken over all positive values of $\omega_1, \omega_2, \omega_3$. The kernel of the integral is

$$S(\omega, \omega_1, \omega_2, \omega_3) = \min(\sqrt{\omega}, \sqrt{\omega_1}, \sqrt{\omega_2}, \sqrt{\omega_3}). \quad (11)$$

Making use of $\delta_{1\omega}^{23}$, and defining $n_c(t) = n(\omega_2 + \omega_3 - \omega, t)$, $S_{\omega}^{23} = S(\omega, \omega_2 + \omega_3 - \omega, \omega_2, \omega_3)$ and $\Delta_{\omega} = \{(\omega_2, \omega_3) : \omega_2, \omega_3 \geq 0, \omega_2 + \omega_3 \geq \omega\}$, one can do further simplifications of the WKE. Finally, it reduces to

$$\frac{d}{dt}n_{\omega} = \eta_{\omega}(t) - n_{\omega}(t)\gamma_{\omega}(t), \quad (12)$$

where

$$\eta_{\omega}(t) = \frac{4\pi^3}{\sqrt{\omega}} \int_{\Delta_{\omega}} S_{\omega}^{23} n_c n_2 n_3 d\omega_2 d\omega_3, \quad (13)$$

$$\gamma_{\omega}(t) = \frac{4\pi^3}{\sqrt{\omega}} \int_{\Delta_{\omega}} S_{\omega}^{23} [n_c(n_2 + n_3) - n_2 n_3] d\omega_2 d\omega_3. \quad (14)$$

Equation (12) conserves the density of particles,

$$N = 2\pi \int_0^{\infty} \omega^{1/2} n_{\omega} d\omega, \quad (15)$$

and the density of linear-dynamics energy,

$$H = H_2 = 2\pi \int_0^{\infty} \omega^{3/2} n_{\omega} d\omega. \quad (16)$$

Note that in WWTT the nonlinear-dynamics energy drops out from the invariant (5). This is natural because by construction it is much smaller than the linear-dynamics energy.

In what follows we shall also need the one-dimensional (1D) waveaction and energy spectra defined respectively as

$$n^{1D}(k, t) = \int n_{\mathbf{k}}(t) k^2 d\Omega, \quad (17)$$

$$E^{1D}(k, t) = \int n_{\mathbf{k}}(t) k^4 d\Omega = k^2 n^{1D}(k, t), \quad (18)$$

where $d\Omega$ is the surface element of the unit sphere in the 3D \mathbf{k} -space.

Note that the densities of total number of particles and linear energy satisfy the relations

$$N = \int_0^{\infty} n^{1D}(k, t) dk \quad \text{and} \quad H_2 = \int_0^{\infty} E^{1D}(k, t) dk.$$

C. Wave turbulence description beyond the spectrum

It has been widely believed that the statistics of random weakly nonlinear wave systems is close to being Gaussian. Derivation of the evolution equation for the probability distribution function (PDF) of the wave intensities presented in [10] has made it possible to examine this belief. It was shown in [10] that this equation indeed has a stationary solution corresponding to the Gaussian state, but it was also noted that the typical evolution time of the PDF is the same as the one for the spectrum. Thus, for non-stationary wave systems one can expect significant deviations from the Gaussianity if the initial wave distributions are non-Gaussian. Note that non-Gaussian (usually deterministic) initial conditions for the wave intensity are typical in numerical simulations in WT. Also, there is no reason to believe that initial waves excited in natural conditions, e.g. sea waves excited by wind, should be Gaussian. Therefore, to study of evolution of the wave statistics is important for both understanding of fundamental nonlinear processes and for the practical predictions such as e.g. wave weather

forecast.

In the present paper we shall use the full general solution for the PDF equation derived in [20] and also the expressions for the moments and cumulants of PDF from [8]. Here, we briefly summarize the results of references [8, 10] and [20].

Let us consider the PDF $\mathcal{P}(s_{\mathbf{k}}, t)$ of the wave intensity $J_{\mathbf{k}} = |a_{\mathbf{k}}|^2$ defined in a standard way, namely, the probability for $J_{\mathbf{k}}$ to be in the range from $s_{\mathbf{k}}$ to $s_{\mathbf{k}} + ds_{\mathbf{k}}$ is $\mathcal{P}(s_{\mathbf{k}}, t)ds_{\mathbf{k}}$. In symbolic form,

$$\mathcal{P}(s_{\mathbf{k}}, t) = \langle \delta(s_{\mathbf{k}} - J_{\mathbf{k}}) \rangle. \quad (19)$$

Under the same assumptions of RPA and weak nonlinearity as the ones used for WKE derivation, the following evolution equation for $\mathcal{P}(s_{\mathbf{k}}, t)$ was derived in [10],

$$\frac{\partial \mathcal{P}(s_{\mathbf{k}}, t)}{\partial t} + \frac{\partial F}{\partial s_{\mathbf{k}}} = 0, \quad (20)$$

where

$$F = -s_{\mathbf{k}} \left(\gamma_{\mathbf{k}} \mathcal{P} + \eta_{\mathbf{k}} \frac{\partial \mathcal{P}}{\partial s_{\mathbf{k}}} \right) \quad (21)$$

and, for the four-wave systems arising from the GPE,

$$\eta_{\mathbf{k}}(t) = 4\pi \int \delta(\mathbf{k} + \mathbf{k}_1 - \mathbf{k}_2 - \mathbf{k}_3) \delta(\omega_{\mathbf{k}} + \omega_{\mathbf{k}_1} - \omega_{\mathbf{k}_2} - \omega_{\mathbf{k}_3}) n_{\mathbf{k}_1} n_{\mathbf{k}_2} n_{\mathbf{k}_3} d\mathbf{k}_1 d\mathbf{k}_2 d\mathbf{k}_3, \quad (22)$$

$$\gamma_{\mathbf{k}}(t) = 8\pi \int \delta(\mathbf{k} + \mathbf{k}_1 - \mathbf{k}_2 - \mathbf{k}_3) \delta(\omega_{\mathbf{k}} + \omega_{\mathbf{k}_1} - \omega_{\mathbf{k}_2} - \omega_{\mathbf{k}_3}) \left[n_{\mathbf{k}_1} (n_{\mathbf{k}_2} + n_{\mathbf{k}_3}) - n_{\mathbf{k}_2} n_{\mathbf{k}_3} \right] d\mathbf{k}_1 d\mathbf{k}_2 d\mathbf{k}_3. \quad (23)$$

Note that in terms of $\eta_{\mathbf{k}}$ and $\gamma_{\mathbf{k}}$, the WKE (9) reads $\frac{d}{dt} n_{\mathbf{k}} = \eta_{\mathbf{k}} - \gamma_{\mathbf{k}} n_{\mathbf{k}}$. In the isotropic case, $\eta_{\mathbf{k}} = \eta_{\omega}$ and $\gamma_{\mathbf{k}} = \gamma_{\omega}$ as defined in (13) and (14).

It is important to realize that generally the PDF evolves at the same time scale τ_{kin} than the spectrum, namely $\tau_{kin} \sim \min(1/\gamma, n/\eta)$. Exceptional are the cases, when either the spectrum is close to a stationary one (e.g. KZ spectrum) or the cases the PDF is close to the stationary one (corresponding to the Gaussian wave fields). In the former case the spectrum evolution time becomes very large, but not necessarily the PDF evolution time, and in the latter case – vice versa.

Laplace transform of equation (20) converts it into a first-order partial differential equation (PDE), which can be solved by the method of characteristics. Moreover, this PDE is linear with respect to \mathcal{P} if we consider spectrum $n_{\mathbf{k}}(t)$ given (i.e. found by solving the WKE first). These facts were used in [20], and the general time-dependent solution of the equation (20) for PDF is obtained there for arbitrary initial statistics.

The solution is constructed at a fixed wave number, so we shall drop the subscripts \mathbf{k} for simplicity. Let us introduce the Green's function $\mathcal{P}_J(s, t)$, i.e. the solution evolving from the initial condition $\mathcal{P}(s, 0) = \delta(s - J)$,

which corresponds to the deterministic initial wave intensity. The general solution with an arbitrary initial condition $\mathcal{P}(s, t)$ is thus given by

$$\mathcal{P}(s, t) = \int_0^{\infty} \mathcal{P}(J, 0) \mathcal{P}_J(s, t) dJ. \quad (24)$$

Using the Laplace transform and the method of characteristics, the following solution was obtained in [20],

$$\begin{aligned} \mathcal{P}_J(s, t) &= \frac{e^{-\frac{s}{\tilde{n}} - a\tilde{n}}}{2\pi i \tilde{n}} \lim_{T \rightarrow +\infty} \int_{T-i\infty}^{T+i\infty} \frac{e^{s\rho + \frac{a}{\rho}}}{\rho} d\rho \\ &= \frac{1}{\tilde{n}} e^{-\frac{s}{\tilde{n}} - a\tilde{n}} I_0(2\sqrt{as}), \end{aligned} \quad (25)$$

where

$$\tilde{n} = n(t) - J e^{-\int_0^t \gamma(t') dt'}, \quad (26)$$

$n(0) = J$, $a = \frac{J}{\tilde{n}^2} e^{-\int_0^t \gamma(t') dt'}$ and $I_0(x)$ is the zeroth modified Bessel function of the first kind.

This is a general solution for an arbitrary initial PDF, but we emphasize that $n(t)$ is considered given. Thus, finding the PDF is a two-step process: first, one has to find $n_{\mathbf{k}}(t)$ by solving the WKE (usually numerically), and

second, substitute the result into the above formula for the analytical solution.

Note that for Gaussian wave fields the PDF of the wave intensities is $\mathcal{P}_G = \frac{1}{n}e^{-s/n}$. As shown in [20], solution (24), (25) implies that (A) the fields, which are Gaussian initially, will remain Gaussian for all time, and (B) at each fixed s wave turbulence asymptotically becomes Gaussian if

$$\lim_{t \rightarrow \infty} \frac{n(0)e^{-\int_0^t \gamma(t')dt'}}{n(t)} = 0. \quad (27)$$

Indeed, taking into account that $I_0(0) = 1$, we recover that $\mathcal{P}_J \rightarrow \mathcal{P}_G = \frac{1}{n}e^{-s/n}$ as $t \rightarrow \infty$, if condition (27) is satisfied provided that $as \ll 1$. Notice also that $a(t) \rightarrow 0$.

It is interesting that the rate of convergence to Gaussianity is greater at those k 's where the initial spectrum is smaller. Indeed, in the limit $J = n(0) \rightarrow 0$ we have $\tilde{n} \rightarrow n$, and $a \rightarrow 0$, so that $\mathcal{P}_J \rightarrow \mathcal{P}_G = \frac{1}{n}e^{-s/n}$.

On the other hand, for large t and $as \gg 1$, taking into account that $I_0(x) \xrightarrow{x \rightarrow \infty} \frac{e^x}{\sqrt{2\pi x}}$, we have

$$\mathcal{P}_J(s, t) \rightarrow \frac{\mathcal{P}_G}{(2\pi)^{1/2}(as)^{1/4}} e^{2\sqrt{as}-as} \ll \mathcal{P}_G. \quad (28)$$

Thus, there is a front at $s \sim s^*(t) = 1/a$ moving toward large s as $t \rightarrow \infty$. The PDF ahead of this front is depleted with respect to the Gaussian distribution, whereas behind the front it asymptotes to Gaussian. Similar behaviour will be realised for any solution (24) evolving from an initial PDF whose decay at large s is faster than exponential.

Further we shall also consider the moments

$$M^{(p)} = \langle |a|^{2p} \rangle \quad (p = 1, 2, 3, \dots),$$

so that the spectrum $n_{\mathbf{k}}$ is represented by the first moment ($p = 1$), whereas the higher moments contain information about fluctuations of the waveaction spectrum about its mean value. For example, for the standard deviation we have

$$\sigma = (\langle |a|^4 \rangle - \langle |a|^2 \rangle^2)^{1/2} = (M^{(2)} - (M^{(1)})^2)^{1/2}. \quad (29)$$

If the wave amplitudes are deterministic, then $M^{(p)} = (M^{(1)})^p$ and $\sigma = 0$. For the opposite extreme of large fluctuations we would have $M^{(p)} \gg (M^{(1)})^p$, which means that the typical realization is sparse in the k -space and is characterized by few intermittent peaks.

For Gaussian fields $M^{(p)} = p! (M^{(1)})^p$. To study the deviations from Gaussianity, it is useful to look at the relative cumulants

$$F^{(p)} = \frac{M^{(p)} - p! (M^{(1)})^p}{p! (M^{(1)})^p}, \quad p = 1, 2, 3, \dots \quad (30)$$

By definition, $F^{(1)}$ is always zero. For $p = 2$, this expression measures the flatness of the distribution of Fourier amplitudes at each k . It determines the r.m.s. of the

fluctuations of the waveaction $\sigma^2 = M^{(2)} - (M^{(1)})^2 = (M^{(1)})^2(2F^{(2)} + 1)$.

The general solution for the relative cumulants can be obtained either from the general solution for the PDF, (24), (25), or by direct derivation of these quantities using WWTT, as it was done in [8]. The result is

$$F^{(p)}(t) = e^{-p\theta} \sum_{j=2}^p \frac{\theta^{p-j} p!}{j!(p-j)!} F^{(j)}(t=0), \quad (31)$$

where $\theta = \int_0^t \frac{n}{n} dt'$ is an effective time variable. One can see that expression (31) decays as $t \rightarrow \infty$ for any fixed p , provided that $\theta \rightarrow \infty$. This condition for approaching to Gaussianity is equivalent to the respective condition for the PDF solution, (27).

It was noted in [8] that, even if the $F^{(p)}$ eventually decay to zero at each *fixed* p , their initial values propagate in p without decay toward the larger values of p . This effect is interconnected with the propagation of the PDF front toward larger s , which we discussed before.

Below, we are going to report on the numerical simulations of the GPE and the WKE, in which the described above predictions about the PDF and the relative cumulants will be put to test alongside the comparisons of the wave spectra.

III. NUMERICAL METHODS

A. Gross-Pitaevskii equation

The GPE (1) is a partial differential equation with a cubic nonlinearity, which is integrated with the pseudo-spectral code FROST. In the triply-periodic box the complex field $\psi(\mathbf{r}, t)$ is represented on the grid of $N_p \times N_p \times N_p$ points. We evaluate the linear terms in Fourier space and the nonlinear term in real (physical) space, which we then transform to Fourier space. The classical 1/3 rule is used for dealiasing. The parallelization of the code uses the interface of MPI communication and standard Fast Fourier Transforms (FFT) of the FFTW library. The library distributes the computation on various processors in dividing the domain into slices. For very large resolutions, a partially hybrid scheme is implemented, in addition with the OpenMP shared memory library. This scheme allows to use more processors at fixed resolutions. One can find more details about the FROST code in [21].

For integration on GPE with respect to time variable, we employ the exponential time differencing Runge-Kutta scheme of fourth order (ETD4RK) (see [22]). In contrast to the classical Runge-Kutta scheme it provides good precision of approximation for both dissipative and dispersive partial differential equations (e.g., GPE as the latter), especially at the smallest scales of the Fourier space.

In the Fourier space we compute 1D waveaction spectra $n^{1D}(k, t)$ defined by equation (17) using its discrete

space version:

$$n^{1D}(k, t) = \frac{1}{D_k} \sum_{\mathbf{k} \in \Gamma_k} |\hat{\psi}(\mathbf{k}, t)|^2. \quad (32)$$

Here, Γ_k is the spherical shell around $|\mathbf{k}| = k$ with the thickness of D_k , where D_k equal to the mesh size $2\pi/L$ (spacing between the grid points in the Fourier space).

We run the code with resolutions $N_p = 128, 256$ and 512 and fix the maximum $|\mathbf{k}|$ to be k_{cutoff} , so that the sizes of box are $L = 2\pi, 4\pi$ and 8π , respectively. For each spatial resolution, an appropriate constant time step is set, such that the relative variation of the global invariants is less than 10^{-4} .

A comment is due on the procedure of averaging in the GPE simulations. Strictly speaking, for computing the ensemble averaged spectrum and the PDF of $J_{\mathbf{k}}$ generated by the GPE, one should perform a large number of numerical simulations starting from independent random initial fields. Performing such a task is unrealistic because it would require computational resources which are far beyond the ones presently available. Instead of this, thanks to the statistical isotropy, we get the statistical averaging via using all wavevectors contained in a given spherical shell in the spectral space.

B. Wave-kinetic equation

The WKE is solved numerically by adapting the method developed in [6] and by applying a second order Runge–Kutta scheme for time marching. The integrals of the collision term are computed using decomposition of the domain of integration into bounded subdomains, inside of which the integrands are highly-smooth functions. Each subdomain is mapped to the reference square, where we construct special grids. Coordinates of nodes of these grids are zeroes of Chebyshev polynomials. Then, we adapt and modify the Clenshaw–Curtis quadrature to compute the integrals on such grids. This method is well suited for the collisional kernel of the GPE based WKE. High accuracy and efficiency of it is reported in [6].

For approximating the spectra on the specified range $[\omega_{\min}, \omega_{\max}] \subset [0, \infty)$ we use the barycentric interpolation formula with Chebyshev nodes. In our study we set $\omega_{\min} = 0.1^2$, $\omega_{\max} = 86^2$. The generalization of barycentric formula to the class of rational approximations is used as well. Such a method enables one to resolve possible singularities of spectra. More details on this issue can be found in Appendix B.

Numerical solutions of the WKE are defined on a grid presenting a scale separation of almost six decades in ω . The time step and the space grid are adjusted in order to ensure a good conservation of invariants. To address the issue of conservation, let us remind that the solution of the WKE is predicted to blow up at $\omega = 0$ at a finite time t^* [1–3, 6], which was estimated in our numerical tests as $t^* \approx 126.7$. For the times $t \in [0, 100]$, which are far

from t^* , we used the grid with 128 nodes. The maximum relative deviations of the particle and energy densities from their initial values are 4.7×10^{-5} and 7.6×10^{-4} , respectively. This non-conservation is mainly due to the leak of particles and energy through the boundary ω_{\max} . To compute the spectrum at the time $t = 125.7$, which is rather close to t^* (see Figure 6), we use a much finer grid with 1024 nodes and expand the segment $[\omega_{\min}, \omega_{\max}]$ to $[0.001, 100^2]$ in order to reduce the leak. In this case the biggest non-conservation 3.69×10^{-4} is observed for the particle density. However, it is worth noting that this small non-conservation of the total particle number is accompanied with rather large approximation error, of the order 15%, in the point-wise values of the wave action spectrum in the vicinity of ω_{\min} . This error is estimated by comparing the 1024 and 512 results. This leads to conclusion that at the moment $t = 125.7$, i.e. rather close to the blow-up t^* , our method still provides an adequate description. More details are available in Appendix B.

Finally, to compare solutions of the WKE with those of the GPE, we notice that

$$n^{1D}(k, t) = 4\pi\omega n_{\omega}(t), \quad (33)$$

where the dispersion relation $\omega = k^2$ was used.

C. Probability distribution functions

We shall concentrate our attention on the case when the initial amplitudes are deterministic, so that the PDF is given by the Green's function $\mathcal{P}_J(t, s)$. We shall also consider the isotropic WT and examine the solutions at several different $k = |\mathbf{k}|$. Before computing $\mathcal{P}_J(t, s)$ for a given k by formula (25), it is convenient to normalize the PDF, so that the first moment of the new variable is equal to unity. Here we introduce the normalized PDF $\tilde{\mathcal{P}}_J(t, \tilde{s}) = \langle s \rangle \mathcal{P}_J(t, \tilde{s} \langle s \rangle)$ with the new stochastic variable $\tilde{s} = s / \langle s \rangle$, where $\langle s \rangle$ represents the ensemble average of intensity $J_{\mathbf{k}}$ at time t . After this normalization the PDF corresponding to the Gaussian statistics becomes $\mathcal{P}_G(\tilde{s}) = \exp(-\tilde{s})$.

To compute the normalized PDF $\tilde{\mathcal{P}}(t, \tilde{s})$, we first solve the WKE numerically using the algorithm described in section III B, and then use the found spectrum to compute $\mathcal{P}_J(t, s)$ using (25). To compute the temporal integral of $\gamma(t')$ in (26), we use a Gaussian quadrature formula with 9 nodes. We carefully check that the PDF is properly normalized, and the mean of \tilde{s} is 1 up to an error smaller than 3×10^{-4} .

IV. NUMERICAL RESULTS

The simulations of both GPE and WKE start with the following initial waveaction spectra of Gaussian shape,

$$n^{1D}(k, 0) = g_0 \exp\left(\frac{-(k - k_s)^2}{\sigma^2}\right). \quad (34)$$

The values of parameters k_s , σ are chosen in such a way that the spectrum has enough space to spread to the left before building up strong condensate at the zero mode. On the other hand, k_s should not be too large that the direct cascade can evolve for significantly long time before the right front of spectrum touches k_{cutoff} — the right boundary of computational domain in the Fourier space. For these reasons, we set $g_0 = 1$, $k_s = 22$, $\sigma = 2.5$ and $k_{\text{cutoff}} = 43$ in the present work.

For WKE, we set $n_\omega(0) = n^{1D}(k, 0)/4\pi\omega$ with $\omega = k^2$.

For GPE, we set $\hat{\psi}_{\mathbf{k}}(0) = |\hat{\psi}_{\mathbf{k}}(0)| \exp(i\phi_{\mathbf{k}}(0))$ with deterministic initial amplitudes $|\hat{\psi}_{\mathbf{k}}(0)| = \sqrt{\frac{n^{1D}(k, 0)}{4\pi k^2} \left(\frac{2\pi}{L}\right)^3}$ and random initial phases $\phi_{\mathbf{k}}(0)$ uniformly distributed in $[0, 2\pi)$ and statistically independent for each \mathbf{k} . Such initial setting for GPE makes the RPA assumption satisfied at $t = 0$ and also corresponds to the initial PDF of intensities $J_{\mathbf{k}} = |\hat{\psi}_{\mathbf{k}}|^2$ being a δ -function.

A. GPE and WKE comparison for the short time evolution

1. Spectrum evolution

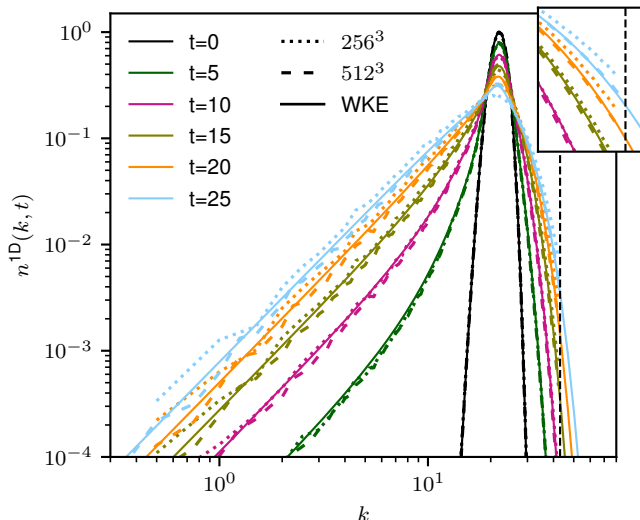


FIG. 1: Time evolution of $n^{1D}(k, t)$ for short time. Results for GPE with 256^3 and 512^3 resolutions and

WKE at times $t = 0, 5, 10, 15, 20, 25$. The vertical dashed line marks the cut-off wave number for GPE numerics, $k_{\text{cutoff}} \approx 43$.

Let us compare the 1D waveaction spectra, $n^{1D}(k, t)$, from the GPE and the WKE simulations. The temporal evolution of $n^{1D}(k, t)$ is plotted in Figure 1. First of all, we observe that the solutions of the GPE and the WKE agree well until $t = 25$. Of course, the results of GPE obtained with 512^3 resolution show better agreement with WKE than the results with 256^3 resolution.

At small k 's, the inverse cascade of the GPE solution obtained with 256^3 resolution is initially slightly slower ($t < 10$), and then slightly faster ($t > 10$) than the inverse cascade of the WKE solution, whereas the spectra obtained from the GPE using 512^3 resolution keep closely behind the ones of the WKE. In the ultraviolet region — for large k 's — the solutions of GPE with 256^3 and 512^3 resolutions start notably deviating from $t = 20$, and the former deviates also from the solutions of the WKE. This can be seen from the zoomed plot presented at the right top corner of Figure 1. The vertical dashed line in Figure 1 indicates the cut-off wave number used in numerical method of solving the GPE, $k_{\text{cutoff}} \approx 43$. The cut-off wave number of the WKE is twice larger than the one of the GPE: $k_{\text{max}} = \sqrt{\omega_{\text{max}}} = 2k_{\text{cutoff}} \approx 86$.

Despite the remarkable agreement of the temporal evolution of the GPE and the WKE waveaction spectra, some minor differences appears at large scales (small k 's), probably due to the k -space discreteness. In order to give a more quantitative comparison between the solutions of the GPE and the WKE, we compute the waveaction and energy based centroids K_N and K_E and their respective typical widths Δ_{K_N} and Δ_{K_E} in the interval $[0, k_{\text{cutoff}}]$ as follows

$$K_N(t) = \frac{1}{N_c(t)} \int_0^{k_{\text{cutoff}}} k n^{1D}(k, t) dk,$$

$$\Delta_{K_N}(t) = \sqrt{\frac{1}{N_c(t)} \int_0^{k_{\text{cutoff}}} (k - K_N)^2 n^{1D}(k, t) dk},$$

$$K_E(t) = \frac{1}{H_c(t)} \int_0^{k_{\text{cutoff}}} k E^{1D}(k, t) dk,$$

$$\Delta_{K_E}(t) = \sqrt{\frac{1}{H_c(t)} \int_0^{k_{\text{cutoff}}} (k - K_E)^2 E^{1D}(k, t) dk}.$$
(35)

In the above definitions, $E^{1D}(k, t) = k^2 n^{1D}(k, t)$ is the 1D linear-dynamics energy spectrum for both WKE and GPE; $N_c(t) = \int_0^{k_{\text{cutoff}}} n^{1D}(k, t) dk$ and $H_c(t) = \int_0^{k_{\text{cutoff}}} E^{1D}(k, t) dk$ are the densities of number of particles and the linear-dynamics energy distributed in $[0, k_{\text{cutoff}}]$ respectively. For the GPE, $N_c(t) = N$ is constant, but $H_c(t) = H_2(t)$ varies around 1% at $t = 25$ (because GPE conserves the density of total energy H including the nonlinear-dynamics energy). For the WKE, $N_c(t)$ and $H_c(t)$ vary, as well, since some waves cascade to modes with $k > k_{\text{cutoff}}$.

Figure 2 shows the dynamics of the centroids and the typical widths for $t \in [0, 25]$. These quantities obtained by solving the WKE and the GPE with resolutions 128^3 , 256^3 and 512^3 . At very short times, $t < 3$, the data obtained from the GPE simulations at all three resolutions and from the WKE demonstrate good agreement. The deviations between the solutions of the GPE with resolutions 256^3 and 512^3 remain rather small until much later times, $t \sim 25$. Since a good accuracy is obtained by solving the GPE with 512^3 resolution, in what follows all the GPE results are given with this resolution.

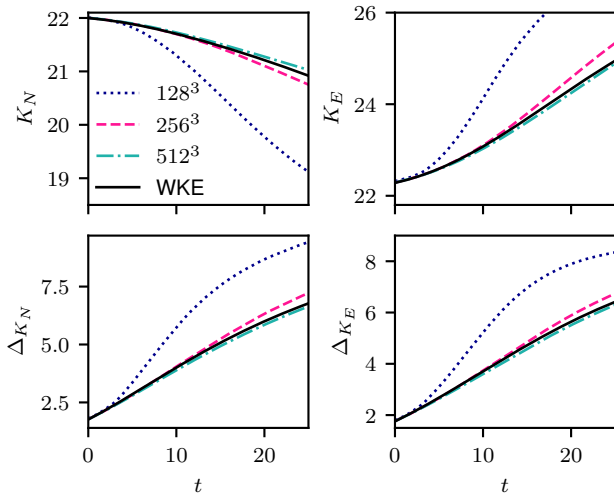


FIG. 2: Dynamics of the centroids of $n^{1D}(k, t)$ and $E^{1D}(k, t)$ and their respective typical widths ΔK_N and ΔK_E for short time, $t \in [0, 25]$. Results for the GPE with 128^3 , 256^3 and 512^3 resolutions and for the WKE.

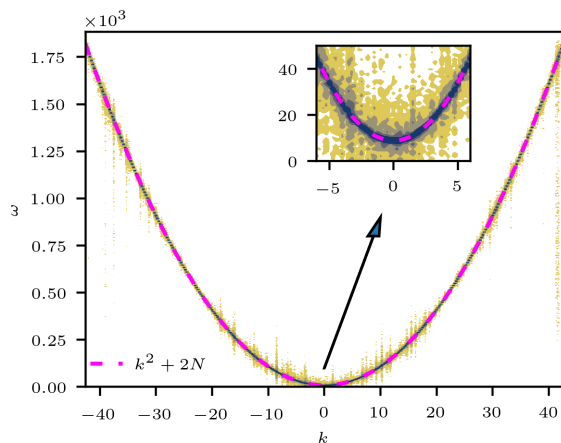


FIG. 3: Spatio-temporal spectral density of $\psi(\mathbf{r}, t)$ over the time interval $[12, 18]$.

2. Verifying the WT assumptions for the GP settings

Here, the assumptions made in section II for the four-wave WWTT will be discussed in the framework of the setup chosen for the GPE simulations. First of all, the condensate fraction C_0 is less than 5×10^{-7} until $t = 25$, and the wave number corresponding to the healing length is $k_\xi = 2.21$. This means that for almost all wave numbers ($k > k_\xi$) the influence of condensation is negligible and the nonlinearity remains small.

We compute the spatio-temporal spectral density of the wave function $\psi(\mathbf{r}, t)$ by performing Fourier transform of $\hat{\psi}(\mathbf{k}, t)$ with respect to the time variable over a finite window of the size T_w . Thanks to the spatial

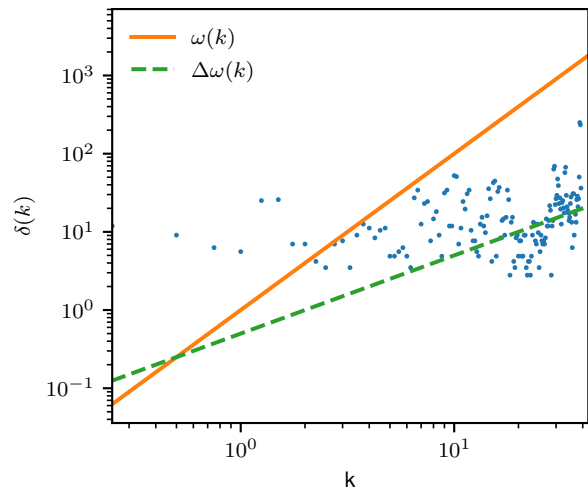


FIG. 4: Frequency broadening $\delta(k)$ (blue points) obtained from the spatial-temporal spectral density over the time interval $[12, 18]$.

isotropy of $\hat{\psi}(\mathbf{k}, t)$, we choose $k_x = k_y = 0$ and perform the Fourier transform in time for each k_z .

Figure 3 displays the normalized spatio-temporal spectral density of $\psi(\mathbf{r}, t)$ over the time interval $t \in [12, 18]$. The normalization is performed along each line $k = \text{const}$ in k - ω plane separately. It consists in division of the spectral density function at the given fixed k by the value of its integral with respect to the variable ω taken over the interval $[0, \infty)$. The figure shows that the majority of the spectrum is concentrated close to the frequencies which satisfy the dispersion relation $\tilde{\omega}(k) = \omega(k) + 2N$ for the corresponding wave numbers, see (8). It should be noted that $\omega(k) = k^2$ is the linear-wave dispersion relation, and $2N$ is the shift induced by the nonlinearity (this shift is shown in the small plot).

Moreover, because of the nonlinearity, a broadening of the frequency can be observed around $\tilde{\omega}(k)$: sufficiently narrow broadening implies weak-wave regime. One can measure the nonlinear frequency broadening $\delta(k)$ directly from the spatial-temporal spectral density. Here, we define $\delta(k)$ for each fixed k in such a way that the integration of the spectral density over the interval of the width $\delta(k)$ centered at the ω -peak gives the value 0.99. To capture such information, the length of the time window T_w of FFT should be larger than both linear and nonlinear time scales, which are $\frac{2\pi}{\omega(k)}$ and $\frac{2\pi}{\delta(k)}$ respectively. Meanwhile, T_w should not be too large so that the spectrum does not vary much over T_w to provide a good accuracy.

Figure 4 presents the frequency of the broadening $\delta(k)$ obtained from Figure 3. We choose the time window $t \in [12, 18]$ around $t = 15$, when the GPE gives good agreement with the WKE. The WWTT, on one hand, requires the nonlinear time scales to be greater than the linear ones, namely, $\delta(k) < \omega(k)$. On the other hand, for solutions of the GPE in the discrete Fourier space to be in

the continuous k -space regime assumed by the WWTT, $\delta(k)$ should be greater than the frequency distance between the adjacent wave modes, $\Delta\omega(k) = 2k\Delta k$. This condition is needed to excite the nonlinear resonant and quasi-resonant interactions among waves (see [7]). One can see that there is a significant k -range for which most of the points (k, δ_k) lay in the domain bounded by $\omega(k)$ and $\Delta\omega(k)$.

It is interesting to see that $\delta(k)$ is greater than $\omega(k)$ at small k 's, which implies strong nonlinearity in the largest scales. However, Figure 1 shows that the waveaction spectrum is small in this range. It reminds us that the “weak wave turbulence” assumption exactly means weakly nonlinear waves rather than weak waves: even if a particular mode is very weak, the linear term at its wave number can be overpowered by the nonlinear term because the former is proportional to the frequency (which is small at small k 's) and the latter is enhanced by contributions from the other modes in the system.

One can also observe in Figure 4 that $\delta(k)$ sinks around $k = 22$ (where the initial waves have maximum amplitudes) and some of the points fall even below the $\Delta\omega(k)$ line. This is because the initial waves generate continuous cascades toward both low and large wave numbers. When $\delta(k)$ falls below the $\Delta\omega(k)$ line, the discreteness of the k -space become significant and deviations from the WWTT should be expected.

Thus we can see in Figure 4 that the range of wave numbers where the WWTT assumptions are satisfied at $t \sim 15$ is, approximately, $2 \lesssim k \lesssim 20$. This range becomes narrower for larger times.

B. GPE and WKE comparison for the long time evolution

In order to study the deviation of the solutions obtained by the GPE and the WKE, we prolong the computations to longer times. In Figure 5 centroids and related typical widths are plotted up to $t = 100$. The centroids of waveaction spectra start to deviate a little earlier than the ones of energy spectra. At late times, the former exhibits larger deviations. The typical widths Δ_{K_N} and Δ_{K_E} show even better correspondence — the curves obtained by the GPE and the WKE go very close until $t \approx 50$.

The comparison of the spectra obtained by solving the GPE and the WKE until $t = 100$ is given in Figure 6. The disagreement between the GPE and the WKE takes place at both low values and high values of k starting around $t = 40$. Overall, the GPE is faster than the WKE for the direct cascade, but slower for the inverse cascade. This trend can be also observed in Figure 5 — the evolution of K_N of the GPE to small k 's is slower than the evolution of K_N of the WKE, whereas the evolution of K_E to large k is faster.

An interesting and important fact is that, even though the GPE is slower than the WKE for small values of

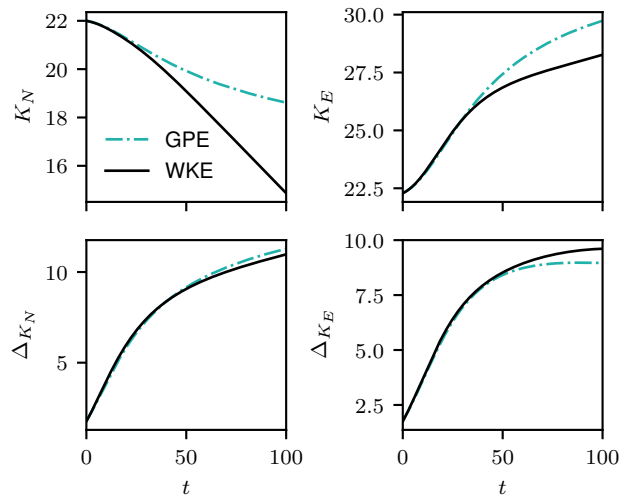


FIG. 5: Dynamics of the centroids of $n^{1D}(k, t)$ and $E^{1D}(k, t)$ and the corresponding typical widths. Results for the 512^3 GPE and the WKE for $t \in [0, 100]$.

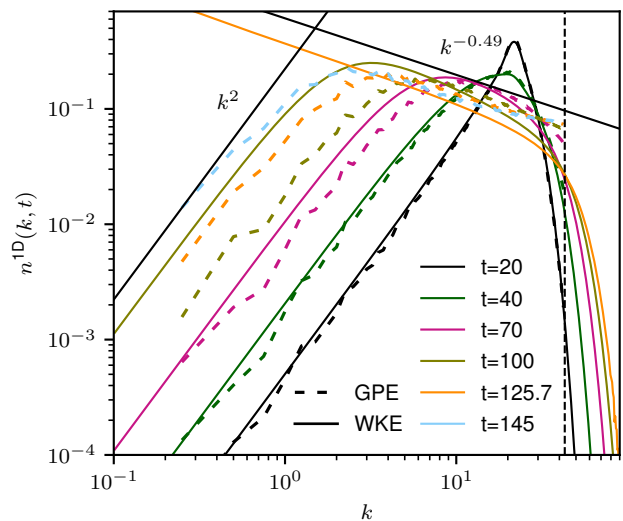


FIG. 6: Long term evolution of $n^{1D}(k, t)$. Results for the 512^3 GPE and the WKE at $t = 20, 40, 70, 100, 125.7$ respectively and for the GPE at 145.

k , both the GPE and the WKE obey the global thermodynamic equilibrium scaling k^2 (the left black solid line), but with different characteristic evolution times. Then considering the long-time evolution, it is important to keep in mind that the solution of the WKE is predicted to blow up at $k = 0$ at a finite time t^* [1–3, 6], so that the WKE cannot be computed beyond this time without a modification of the model taking into account the zero-mode evolution. For the initial condition considered in the present paper, we found numerically that $t^* \approx 126.7$. Close to t^* , the evolution appears to be self-similar, with a transient power law forming in the

inverse cascade $n_k^{\text{ID}} \propto k^{-x^*}$ with exponent x^* which has a different value than the one in the inverse-cascade KZ solution, namely x^* differs from $1/3$. The most careful recent study of the self-similar formulation of the WKE [6] gives two values of x^* for the most accurate solutions, 0.44 and 0.48. Further, a similar behaviour was observed in 512^3 simulations of the 3D GPE with a slightly different value, $x^* \approx 0.52$ [23]. In Figure 6 we see that the late WKE spectra exhibit law $k^{-0.49}$ (indicated by a black solid line) whereas the GPE scaling is slightly less steep, probably due to the spectrum pileup near k_{cutoff} .

Let us now concentrate on the differences that the GPE and the WKE exhibit for the inverse and the forward cascade ranges. It is easy to see that for small wave numbers (i.g. $k < 10$), the curves obtained by the GPE show visible fluctuations starting from $t = 40$, while the results generated by the WKE keep good smoothness all the time. This behaviour is to be expected considering the fact that the WKE deals with ensemble averaged wave distributions and with a space of continuous wave number (allowing for using the grids in k variable, which are finer at low k 's), whereas the GPE spectra are not ensemble (or time) averaged: the only averaging in this case is over spherical shells in the Fourier space, which contain less and less modes as one moves to smaller k 's.

Note that although the WKE can have a finer grid in the vicinity of $k = 0$ than the GPE, this point is excluded from the WKE simulation, but when solving the GPE, it is naturally included. Indeed, while the GPE solution evolves, the condensate fraction C_0 may start to grow. However, in the current simulations its final value is less than 5×10^{-5} at $t = 145$, so the influence of condensate in the GPE simulation still can be neglected. The fact that the WKE predict condensation starting at $t^* \approx 126.7$ whereas no condensate growth is seen in the GPE simulation even at $t = 145$ could be qualitatively understood if we recall the condensation criterion for the weakly interacting 3D GPE: $E/N < k_{\text{max}}^2/3$ [24]. It turns out that for our initial condition this criterion is well satisfied for the WKE but only marginally so for the GPE because the former has a twice bigger cutoff wave number than the later. In a separate simulation we have verified that condensation does indeed occur for the GPE too if the initial spectrum is shifted to smaller wave numbers (leading to smaller E/N). Another possible reason explaining the difference between the GPE and the WKE results at small k 's is the failure of weak wave assumption in this region, as shown in Figure 4.

On the other side, the UV cut-off of the GPE results in accumulating of waves near k_{cutoff} , which affects the overall dynamics of the system. It is difficult to break this restriction in numerical simulations since it is induced by finite computational domain and finite space resolutions. However, the WKE can provide solutions for large values of k with acceptable requirement of computational resources.

C. Low and high order statistics

1. Comparison of the PDFs and the low order cumulants (GPE and WKE)

Let us now consider the PDF of the transient states starting from the deterministic initial amplitudes and evolving towards an exponential PDF corresponding to a Gaussian wave-field statistics. We shall use here the previous setup (34) and analyze the evolution of the normalized PDF and the relative cumulants at the point $k = k_s = 22$ — the maximum point of the initial spectrum, and the points $k = 19$ and $k = 25$ symmetrically placed around $k = 22$. Figures 7 and 8 display the temporal evolution of $\tilde{\mathcal{P}}_J(t, \tilde{s})$ and $F^{(p)}(t)$ respectively. As expected, for all three modes the normalized PDFs for both the GPE and the WKE spectra evolve from the $\delta(\tilde{s} - 1)$ at $t = 0$ to the final exponential distribution $e^{-\tilde{s}}$. Overall, the results generated by the GPE agree well with the prediction derived from the WKE. Also, from Figure 7 we see that the PDF at $k = 22$ evolves towards Gaussianity slower than the PDFs at $k = 19$ and $k = 25$. This consists with our prediction that the rate of convergence to Gaussianity is faster for those k 's where the initial spectrum $n_k(0)$ has smaller values.

Figure 8 provides further validation of the statistical predictions derived from the WKE by plotting the relative cumulants of the first to fifth orders. All the cumulants finally tend to zero—the state corresponding to the Gaussian wave-field statistics (again, faster at $k = 19$ and $k = 25$ than at $k = 22$). For high orders, GPE cumulants start to deviate from those of WKE after reaching a certain time. As explained above, the discreteness of the GPE modes does not allow the degree of averaging sufficient for generating accurate PDF especially for large values of \tilde{s} . The accuracy of high order moments is also affected by such a discretization earlier in time than the accuracy of the low order ones. As a consequence, in Figure 7 for $t = 20$, the GPE gives good picture of $F^{(p)}(t)$ up to the fifth order at $k = 22$, but at $k = 19$ and $k = 22$ good agreement with the WKE is preserved only up to $p = 4$.

2. High-order cumulants from WKE

Studying high-order statistics for a time dependent problem requires to produce ensemble realizations in order to collect the statistics. For the GPE simulations presented in this work, such study is prohibiting. Instead, the WWTT provides a framework in which the high-order statistics can be studied.

We compute numerically the PDFs using the WWTT for long times and focus on their tails. Figure 9a shows the relative PDFs (PDFs normalized by $\mathcal{P}_G = e^{-\tilde{s}}$) computed at $k = 22$. The black dot in Figure 9a denotes the point $\tilde{s} = \tilde{s}^*(t)$ where the curve corresponding to $t = 50$ starts to deviate from the limiting dash line by more than

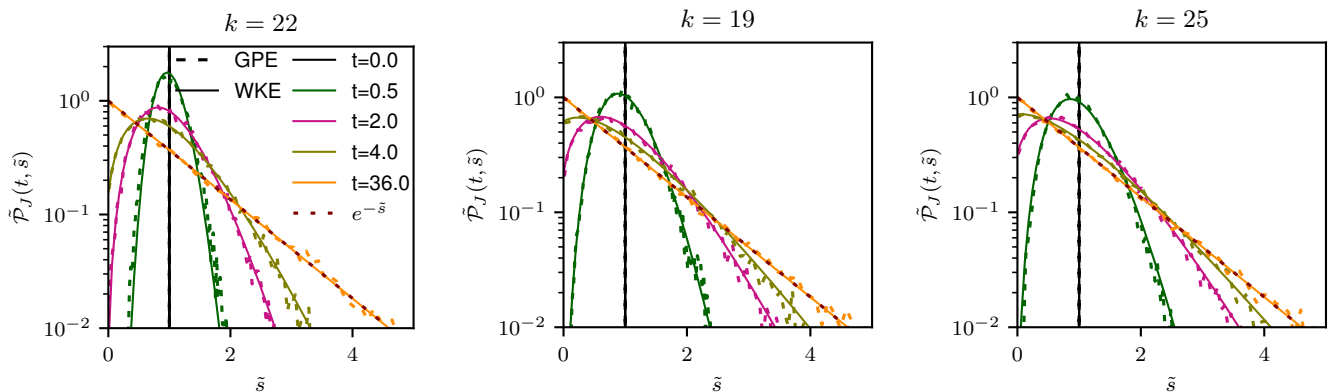


FIG. 7: Time evolution of the normalized probability density functions $\tilde{\mathcal{P}}_J(t, \tilde{s})$. Results for 512^3 GPE and WKE for various k .

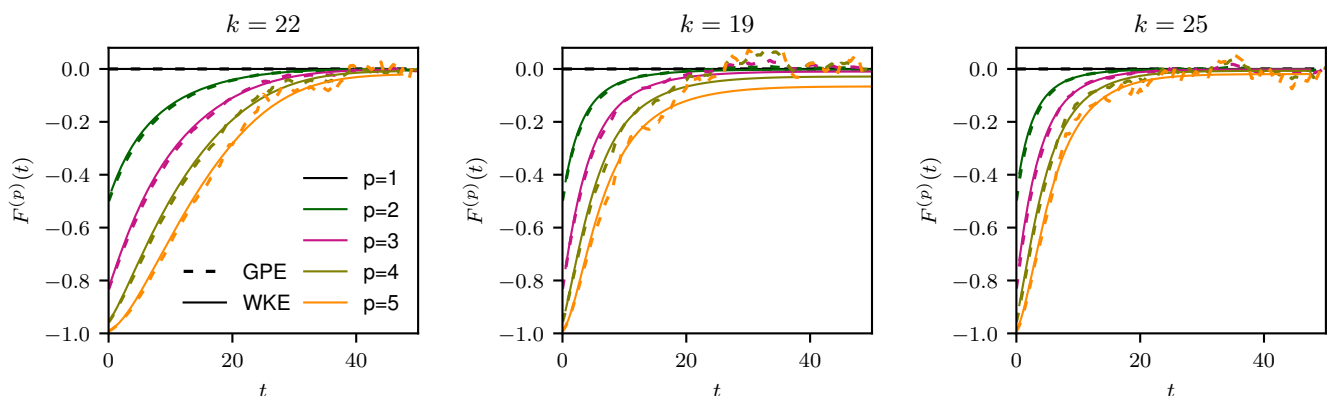


FIG. 8: Time evolution of the relative cumulants $F^{(p)}(t)$. Results for 512^3 GPE and WKE for various k .

1%, i.e. where the ratio of PDF divided by the final exponential form takes the value 0.99. The dynamics of the point $\tilde{s}^*(t)$ illustrates a front moving towards large \tilde{s} as $t \rightarrow \infty$. Behind this front PDF asymptotes to the exponential one, whereas ahead of this point it still deviates by 1%. Figure 9b displays the dynamics of $\tilde{s}^*(t)$ for different values of k , showing its acceleration in the final phase, which depends on the wave number.

Let us now consider the behavior of high order relative cumulants computed using the solution of the WKE and defined as in (30). In Figure 10a the cumulants as functions of the order p are shown at different times for $k = 22$. Similarly, the point $p^*(t)$ corresponds to the value of p for which at the time moment t the cumulant $F_k^{(p)}$ takes the value -0.01 . Figure 10b shows the propagation of front associated with the motion of the point $p^*(t)$.

We should mention here an obvious similarity between the evolution of relative PDFs as functions of \tilde{s} and of the cumulants as functions of p , when t is large enough.

V. DISCUSSION AND CONCLUSIONS

The main goal of the present paper is to test the weak Wave Turbulence theory (WWTT) by comparing numerical simulations of the Gross-Pitaevskii equation (GPE) and the wave-kinetic equation (WKE). Several fundamental constraints have to be kept in mind during such a comparison.

Firstly, the WWTT assumes that the wave must be weak enough, but not too weak. Namely, the waves have to be weak so that the linear dynamics is faster than the nonlinear transfers of energy between the wave modes, but also strong enough so that the nonlinear frequency broadening is larger than the frequency spacing between the nearby modes in the wave number space, so that the continuous k -space limit can be considered. We have checked these conditions in our numerical simulations. Figure 4 shows that the range of wave numbers, where these two WWTT assumptions are satisfied simultaneously at $t \sim 15$, is $2 \lesssim k \lesssim 20$, and we found that this range becomes narrower for larger times. It is then rather remarkable that we found a nearly perfect agreement be-

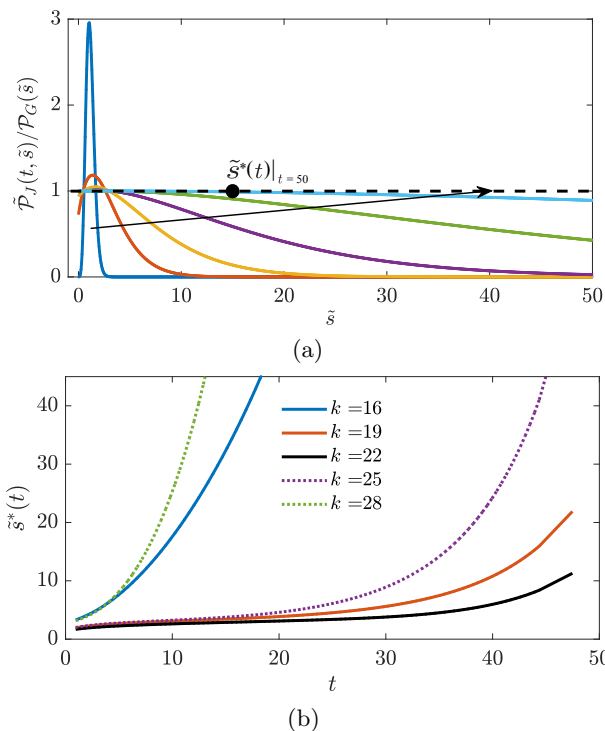


FIG. 9: (a) Relative probability density functions computed using the numerical solutions of WKE for different time moments and $k = 22$. The arrows show time evolution and pass from the left to the right through the curves corresponding to $t = 1, t = 10.8, t = 20.6, t = 30.4, t = 40.1, t = 50$. Horizontal dashed line shows the Gaussian distribution. (b) Motion of the front $\tilde{s}^*(t)$ for different values of k .

tween the WKE and the GPE results up to $t \sim 30$, which is about two nonlinear (kinetic) evolution times (defined as a time needed for the maximum of spectrum to decrease to the half of its initial value). To characterise our comparisons, we have looked directly at the spectra, as well as at their global characteristics – the energy and the particle centroids and typical widths. Another surprising fact is that even relatively low 256^3 resolution of GPE simulations leads to a reasonably accurate agreement between the WKE and the GPE results, even though, naturally, the accuracy is better for 512^3 (and not at all good for 128^3).

We have also looked numerically at the probability density functions (PDFs) of the wave intensities, both using GPE simulations (directly) and WWTT (complementing the WKE simulations with the analytical solution for the PDF obtained in [20]). Here as well, we have seen an excellent agreement for the early evolution up to $t \sim 30$ and, qualitatively, far beyond this time. In fact, in agreement with the theoretical predictions, the PDFs of the wave intensities tend to exponentially decreasing functions corresponding to Gaussian wave fields.

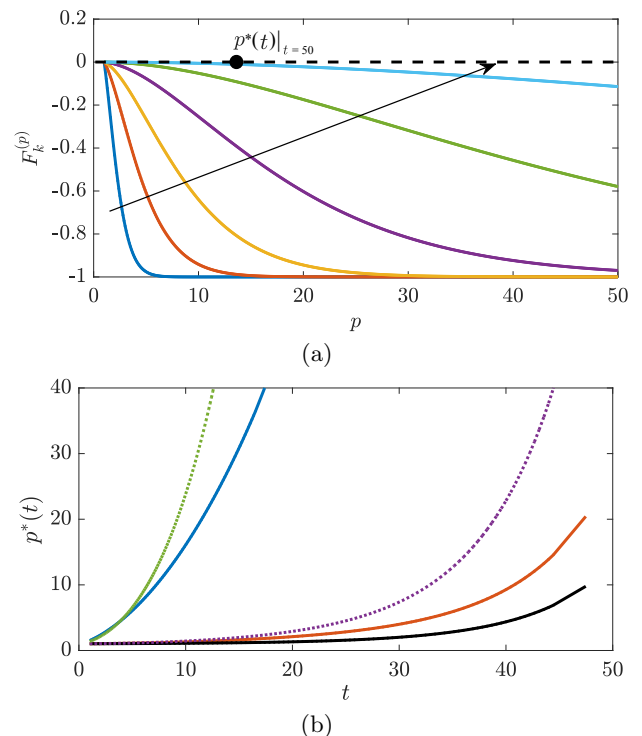


FIG. 10: (a) Cumulants as a function of their order p (same times as in Figure 9.a). (b) Motion of the front $p^*(t)$ for different values of k (as in Figure 9.b). Bottom black line corresponds to $k = k_s$.

At $t \sim 30$, the PDFs have practically attained the final exponential shape, and the only difference between the WWTT and the GPE results is that the PDFs obtained for the GPE have noisy tails due to insufficient averaging. It is important to emphasize that, in agreement with the theoretical predictions [7, 11, 20], the evolution toward Gaussianity occurs at the kinetic timescale (in our case $t \sim 15$) i.e. at the same characteristic time as the one for the spectrum evolution, rather than a much shorter timescale as one could naively believe. Note that evolution of the wave intensity PDF from deterministic to exponential in simulations of 2D GPE was previously observed in [25], where it was reported that PDF evolution time is much faster than the one for the spectrum, which seems at odds with our findings. The contradictions seems to originate from the difference in the definition of the characteristic evolution time for the spectrum: in the present paper we define it as a time needed for the spectrum to experience order-one changes (specifically, for its maximum to become twice smaller) where as a much longer time needed for the spectrum to approach to thermodynamic equilibrium is discussed in [25]. Also, it is not clear if the simulations of [25] were in the WWT regime: evidence about smallness of nonlinearity and absence of the discreteness effects was presented. We would also like to mention a previous study of a model 2D three-wave system [26] where a comparison was made for the

PDF and cumulants obtained from a DNS and the numerics of the WWTT closure equations for these statistical objects (no analytical solution for the PDF was available at that time yet). They arrived at favourable conclusions for validity of the WWTT for the considered three-wave system.

Secondly, WWTT assumes a “propagation of chaos” property: the random phase and amplitude (RPA) statistics of the initial data should survive through the nonlinear (kinetic) evolution time [7, 9, 10]. Naively, one could think that the RPA statistics could be tested numerically by directly accessing the joint statistics of the Fourier modes. However, it is clear that RPA cannot propagate in its pure form for the entire set of the wave modes. Instead, it should survive only in a sense of distributions, e.g. the statistical moments and the reduced PDFs restricted to smaller number of waves [7, 11]. Numerical studies of these issues would be a good subject for future research. In the present work, however, we see an indirect evidence for the propagation of chaos in the fact that WKE provides a good description of the wave spectrum for at least two nonlinear kinetic times.

It is interesting that a qualitative agreement of the GPE and WKE results is also observed to the long-time evolution, up to $t \sim 100$ and even beyond (but obviously for $t < t^*$, where t^* is the finite time moment when the solution of WKE blows up at zero mode). In particular, in both simulations a self-similar inverse cascade with two power-law scalings (with exponents ~ 2 and ~ -0.49) is observed for t close to t^* . However, significant differences arise at the lowest and the highest scales for $t \gtrsim 40$. In addition to the shrinking of the WWTT applicability range, which we mentioned before, the factors causing the deviations include the differences in the minimal and the maximal scales used for the WKE and GPE. Generally, one can afford a much greater range of wave numbers in WKE than in GPE. In our WKE simulations we had the minimal wave number at about 0.1 and the maximal wavenumber – at 86, whereas in 512³ GPE these boundaries were at 0.25 and 43 respectively. Having lower maximum wave number leads to a visible accumulation of spectrum in the highest wave numbers, whereas in the WKE results the forward cascade spreads freely to much higher k 's. It is then surprising that the energy centroid for the WKE appears to move to the right slower than the one for the GPE. It is equally surprising to see the inverse cascade moving toward low k 's faster for WKE and GPE. Indeed, this result is at odds with a common view that the nonlinearity becomes stronger during the inverse cascade process, so the GPE system should switch from the kinetic to a dynamic timescale which is shorter. At present, we do not have an explanation for this behaviour.

VI. ACKNOWLEDGEMENTS

This work is funded by the Simons Foundation Collaboration grant Wave Turbulence (Award ID 651471). Part of this work was granted access to the high-performance computing facilities under GENCI (Grand Equipement National de Calcul Intensif) A0102A12494 (IDRIS and CINES), the OPAL infrastructure from Université Côte d'Azur, supported by the French government, through the UCAJEDI Investments in the Future project managed by the National Research Agency (ANR) under reference number ANR-15-IDEX-01, and the SIGAMM infrastructure (<http://crimson.oca.eu>) hosted by Observatoire de la Côte d'Azur and supported by the Provence-Alpes Côte d'Azur region.

Appendix A: Derivation of the angle-averaged kinetic equation

In the case when the wave fields are statistically isotropic, the averaging of WKE (9) can be done by integrating it over the unit sphere S_1 and performing the internal angle integrations. This will change the variables \mathbf{k} and \mathbf{k}_j , $j = 1, 2, 3$, of (9) to variables $k = |\mathbf{k}|$ and $k_j = |\mathbf{k}_j|$ respectively. In what follows we also use the representations $d\mathbf{k} = k^2 dk d\Omega$ and $d\mathbf{k}_j = k_j^2 dk_j d\Omega_j$, where $d\Omega$ and $d\Omega_j$ are the area elements on the unit spheres associated with the vectors \mathbf{k} and \mathbf{k}_j , respectively. Isotropy of the spectrum means that it depends only on the modulus of the vector \mathbf{k} , i.e. $n_{\mathbf{k}} = n_k$.

Denoting $n_j = n_{\mathbf{k}_j}$, $\omega = \omega_{\mathbf{k}}$ and $\omega_j = \omega_{\mathbf{k}_j}$, one can write the averaged WKE as follows

$$\begin{aligned} \frac{dn_k}{dt} &= \frac{1}{4\pi} \int_{S_1} \frac{dn_{\mathbf{k}}}{dt} d\Omega = \\ &= \int \mathcal{P} \delta_{1\omega}^{23} n_k n_1 n_2 n_3 \left(\frac{1}{n_k} + \frac{1}{n_1} - \frac{1}{n_2} - \frac{1}{n_3} \right) d123, \end{aligned} \quad (\text{A1})$$

where

$$\delta_{1\omega}^{23} = \delta(\omega + \omega_1 - \omega_2 - \omega_3), \quad d123 = k_1^2 k_2^2 k_3^2 dk_1 dk_2 dk_3,$$

$$\mathcal{P} = \int \delta_{1\mathbf{k}}^{23} d\Omega d\Omega_1 d\Omega_2 d\Omega_3, \quad (\text{A2})$$

where $\delta_{1\mathbf{k}}^{23} = \delta(\mathbf{k} + \mathbf{k}_1 - \mathbf{k}_2 - \mathbf{k}_3)$. To compute \mathcal{P} , we first recall that the Dirac δ -function can be represented as the Fourier transform of unity:

$$\delta_{1\mathbf{k}}^{23} = \frac{1}{(2\pi)^3} \int_{\mathbb{R}^3} \exp[-i\mathbf{r} \cdot (\mathbf{k} + \mathbf{k}_1 - \mathbf{k}_2 - \mathbf{k}_3)] d\mathbf{r}, \quad (\text{A3})$$

Therefore, substituting (A3) into (A2) and changing the order of integration one obtains

$$\mathcal{P} = \frac{1}{(2\pi)^3} \int_{\mathbb{R}^3} P(\mathbf{r}) d\mathbf{r}, \quad (\text{A4})$$

where

$$P(\mathbf{r}) = \int \exp[-i\mathbf{r} \cdot (\mathbf{k} + \mathbf{k}_1 - \mathbf{k}_2 - \mathbf{k}_3)] d\Omega d\Omega_1 d\Omega_2 d\Omega_3. \quad (\text{A5})$$

Let us pass to the angular coordinates of spherical surfaces, (φ, θ) , where $0 \leq \varphi \leq 2\pi$, $0 \leq \theta \leq \pi$ (and the same for φ_j, θ_j):

$$d\Omega = \sin\theta d\theta d\varphi, \quad d\Omega_j = \sin\theta_j d\theta_j d\varphi_j, \quad j = 1, 2, 3.$$

Defining θ_j to be to the angles between the vectors \mathbf{k}_j and \mathbf{r} , we have

$$\mathbf{r} \cdot \mathbf{k}_j = rk_j \cos\theta_j, \quad j = 1, 2, 3,$$

where $r = |\mathbf{r}|$. Similarly,

$$\mathbf{r} \cdot \mathbf{k} = rk \cos\theta.$$

Thus, one can write

$$\begin{aligned} \int e^{-i\mathbf{r} \cdot \mathbf{k}} d\Omega &= \int_0^{2\pi} d\varphi \int_{-1}^1 d\chi e^{-irk\chi} = \\ &= \frac{2\pi}{irk} \exp(-irk\chi) \Big|_{\chi=-1}^1 = \frac{4\pi}{rk} \sin(rk), \end{aligned} \quad (\text{A6})$$

where $\chi = \cos\theta$.

Using (A6) and the similar results for the integrals of $e^{-i\mathbf{r} \cdot \mathbf{k}_j}$, $j = 1, 2, 3$, one can write for the integral in (A5):

$$P(\mathbf{r}) = \frac{(4\pi)^4}{r^4} \frac{\sin(rk)}{k} \prod_{i=1}^3 \frac{\sin(rk_i)}{k_i}.$$

$$\frac{dn_k}{dt} = \frac{32\pi^3}{k} \int \min(k, k_1, k_2, k_3) \delta_{1\omega}^{23} n_k n_1 n_2 n_3 \left(\frac{1}{n_k} + \frac{1}{n_1} - \frac{1}{n_2} - \frac{1}{n_3} \right) k_1 k_2 k_3 dk_1 dk_2 dk_3. \quad (\text{A7})$$

The last point, which we shall address here, is passage in (A7) to the frequency variables $\omega = k^2$ and $\omega_j = k_j^2$, $j = 1, 2, 3$. Using the expressions $k = \sqrt{\omega}$, $dk = \frac{1}{2}\omega^{-1/2}$, $k_j = \sqrt{\omega_j}$, $dk_j = \frac{1}{2}\omega_j^{-1/2}$ and denoting $n_\omega = n_k$ and

$$S(\omega, \omega_1, \omega_2, \omega_3) = \min(\sqrt{\omega}, \sqrt{\omega_1}, \sqrt{\omega_2}, \sqrt{\omega_3}),$$

one obtains (10) from (A7).

Appendix B: Extra numerical details for WKE

An important block of the algorithm for solving WKE, which should be mentioned first, is an accurate and fast computation of the collision integral in the RHS of (12). To perform such a computation, the cubature formulas proposed in [6] are applied, which requires

Substituting this into (A4) using the representation $d\mathbf{r} = r^2 dr d\Omega_{\mathbf{r}}$, and using *Mathematica* for integration, we get the following expression,

$$\begin{aligned} \mathcal{P} &= \frac{32\pi}{kk_1 k_2 k_3} \int d\Omega_{\mathbf{r}} \int_0^\infty \frac{\sin(rk)}{r^2} \prod_{j=1}^3 \sin(rk_j) dr = \\ &= \frac{8\pi^3}{kk_1 k_2 k_3} (-|k + k_1 - k_2 - k_3| - |k - k_1 + k_2 - k_3| + \\ &\quad |k + k_1 + k_2 - k_3| - |k - k_1 - k_2 + k_3| + \\ &\quad |k + k_1 - k_2 + k_3| + |k - k_1 + k_2 + k_3| + \\ &\quad |-k + k_1 + k_2 + k_3| - |k + k_1 + k_2 + k_3|). \end{aligned}$$

This expression can be considerably simplified after taking into account the four-wave frequency resonance condition

$$k^2 + k_1^2 = k_2^2 + k_3^2.$$

This leads to

$$\mathcal{P} = \frac{32\pi^3}{kk_1 k_2 k_3} \min(k, k_1, k_2, k_3).$$

Substituting this into (A1), we obtain the angle-averaged WKE:

decomposition of the domain of integration Δ_ω in (13), (14). In our study Δ_ω is represented as $\Omega_1 \cup \Omega_2$, where

$$\Omega_1 = \{(\omega_2, \omega_3) : \omega_2, \omega_3 \geq 0, 0 \leq \omega_2 + \omega_3 \leq \omega_{max}\},$$

$$\Omega_2 = \{(\omega_2, \omega_3) : \omega_2, \omega_3 \leq \omega_{max}, \omega_2 + \omega_3 > \omega_{max}\}.$$

The integrands of RHSs of (13), (14) have singularities along the lines $\omega_2 = \omega$, $\omega_3 = \omega$, $\omega_2 = \omega_{min}$, $\omega_3 = \omega_{min}$, $\omega_2 + \omega_3 = \omega_{min}$, where the first and the higher order derivatives of the integrands can have discontinuities. Therefore, to design cubature formulas with an exponential rate of convergence, Δ_ω must be cut along these lines and decomposed into triangular, rectangular, and trapezoidal subdomains. Inside each subdomain the integrands are infinitely differentiable functions, see [6] and figures 1,2 there. Each of the subdomains is mapped onto

the reference square $[-1, 1]^2$ (see [27] for the additional details), and tensor products of the modified Clenshaw–Curtis formulas are used to compute the integrals. It should be noted that, in contrast to the formulation considered in [6], here we have a bounded domain of integration, which somewhat simplifies the problem.

Now, let us address the problem of approximating the solution of WKE, $n_\omega(t)$. Here, first of all one should choose an appropriate interval of approximation with respect to the variable ω . Since the spectrum vanishes very fast at large ω , it is enough to build approximation on the finite interval $[\omega_{min}, \omega_{max}]$ with large enough ω_{max} and set $n_\omega(t) = 0$ for any $t < T$ and $\omega > \omega_{max}$. One also should take into account that the solution of WKE blows up at the zero mode at some finite time t^* . Moreover, in the vicinity of $t = t^*$ the spectrum demonstrates a self-similar behavior with the shape having plateau for the small values of ω , see [1–3, 6] for details. To exclude the singularity at $\omega = 0$, we choose a small positive ω_{min} and fix $n_\omega(t) = n_{\omega_{min}}(t)$ for any $t < T$ and $\omega < \omega_{min}$. Here, following the above results we set $T = 100$.

For approximating WKE with respect to the time variable, we use the Runge–Kutta method of the order 2 (RK2), introduce the uniform grid with the step dt and the nodes $t_j = jdt$, $j = 0, 1, \dots$ and implement an explicit time-marching scheme. Then, we denote $n^{[j]} = n^{[j]}(\omega) = n_\omega(t_j)$ and approximate the function $n^{[j]}(\omega)$ on the segment $[\omega_{min}, \omega_{max}]$ by the interpolation polynomial with Chebyshev nodes. For this we use the barycentric interpolation formula from [28]:

$$p_M[n^{[j]}](\omega) = \sum_{m=1}^M \frac{\xi_m n^{[j]}(\omega_m)}{\mathcal{L}(\omega) - y_m} \Big/ \sum_{m=1}^M \frac{\xi_m}{\mathcal{L}(\omega) - y_m}, \quad (\text{B1})$$

where $\xi_m = \frac{1}{T_M(y_m)} = (-1)^{m-1} \sin(\frac{2m-1}{2M}\pi)$ are the weights of interpolation; $T_M(y)$ is the Chebyshev polynomial of the degree M ; y_m are zeroes of $T_M(y)$, $m = 1, \dots, M$; $\mathcal{L}(\omega)$ is the linear mapping of the segment $[\omega_{min}, \omega_{max}]$ to $[-1, 1]$; $\omega_m = \mathcal{L}^{-1}(y_m)$ are the interpolation nodes.

We also use the rational variant of (B1), which turns out to be a very efficient way of adapting the approximation to singularities of the solution, see [29, 30]. In our case the singularities are related with a huge length of the considered ω -interval (up to 7 decades) and with the blow-up of the solution at the zero mode. To obtain the rational barycentric interpolation, we fix the weights ξ_m of (B1), but instead of the Chebyshev nodes y_m we use the transformed ones $\tilde{y}_m = g(y_m)$, $m = \overline{1, M}$. Here, the mapping $g : [-1, 1] \rightarrow [-1, 1]$ is bijection, which has an analytical continuation to the complex plain. This continuation must be reversible, and the inverse mapping g^{-1} must take the singular point $\tilde{y}_1^* = \mathcal{L}(0)$ far enough from the segment $[-1, 1]$. Several possibilities of defining $g(y)$ are discussed in [30–32]. However, the straightforward application of these formulas leads to very strong concentration of the nodes in the vicinity of $\omega = 0$ and

bad resolution of the initial Gaussian peak centered at $\omega = k_s^2$.

To take into account both singular points $\tilde{y}_1^* = \mathcal{L}(0)$ and $\tilde{y}_2^* = \mathcal{L}(k_s^2)$, we used the idea from [33], which allows one to write the mapping in the form

$$g = \left(\frac{g_1^{-1} + g_2^{-1}}{2} \right)^{-1},$$

where the superscript “ -1 ” means the inversion of a function; g_1^{-1} , g_2^{-1} serve for mapping the singular points \tilde{y}_1^* and \tilde{y}_2^* , respectively. In our case

$$g_i^{-1}(\tilde{y}) = \frac{a^+ - a^- + 2 \sinh^{-1} \frac{\tilde{y} - \tilde{y}_i^*}{\epsilon_i}}{a^+ + a^-},$$

$$a^\pm = \sinh^{-1} \frac{1 \pm \tilde{y}_i^*}{\epsilon_i},$$

where $i = 1, 2$, ϵ_1, ϵ_2 are the small positive parameters used for tuning the densities of concentration of nodes in the vicinities of \tilde{y}_1^* and \tilde{y}_2^* , respectively. The closer $\epsilon_{1,2}$ are to zero, the higher is the density of the concentration. Basically, we set $\epsilon_1 = 10^{-4}$, $\epsilon_2 = 10^{-1}$. It is worth noting that these parameters also have an important mathematical meaning. For the details about this issue we refer the reader to [30, 31]. The described mapping g in combination with the barycentric representation (B1) allows one to achieve the high accuracy even using coarse grids. However, it also requires for some modifications of the formulas for integrating the obtained spectra.

For computing the centroids by formulas (35) we first make the change of the variable $k = \sqrt{\omega}$, then use the mapping $\omega = \mathcal{L}^{-1} \circ g(y)$ with the Jacobian

$$J_{\mathcal{L}g}(y) = \frac{\omega_{max} - \omega_{min}}{1/(g_1' \circ g_1^{-1} \circ g(y)) + 1/(g_2' \circ g_2^{-1} \circ g(y))},$$

and, finally, for integration with respect to the variable $y = g^{-1} \circ \mathcal{L}(\omega)$ we used the Clenshaw–Curtis formulas, see [34].

In numerical tests we checked the convergence of the proposed method by observing the quantity

$$R_M(n) = R_{M,t}(n) = \frac{\max_{\omega} |n_M(\omega, t) - n_{2M}(\omega, t)|}{\max_{\omega} |n_{2M}(\omega, t)|}$$

obtained in computations with the fixed and small enough value of the time step dt , where $n_M(\omega, t) = p_M[n^{[j]}](\omega)$ is the rational interpolation of the spectrum with M nodes, see (B1). Here, it is assumed that for computing the collision integral we use the cubature formulas with M^2 nodes in each subdomain of Ω . We also computed the quantities

$$R_M(\varkappa) = R_{M,t}(\varkappa) = \frac{|\varkappa_M(t) - \varkappa_{2M}(t)|}{\varkappa_{2M}(t)},$$

where \varkappa denotes one of the functions $K_N(t)$, $K_E(t)$, $\Delta_{K_N}(t)$, $\Delta_{K_E}(t)$ determined in (35), and the subscript

M stands for the number of nodes of spatial grid used for the approximation of the solution and for the number of nodes of all the applied formulas for numerical integration.

By analogy we computed the values

$$R_{dt}(n) = R_{dt,t}(n) = \frac{\max_{\omega} |n_{dt}(\omega, t) - n_{dt/2}(\omega, t)|}{\max_{\omega} |n_{dt/2}(\omega, t)|}$$

with the fixed and large enough number of space nodes, where $n_{dt}(\omega, t)$ is the solution obtained using RK2 with the time step dt . As well, we computed the values

$$R_{dt}(\varepsilon) = R_{dt,t}(\varepsilon) = \frac{|\varepsilon_{dt}(t) - \varepsilon_{dt/2}(t)|}{|\varepsilon_{dt/2}(t)|},$$

where $\varepsilon_{dt}(t)$ is determined similarly to $n_{dt}(\omega, t)$.

In Tables I, II the values of R_M and R_{dt} are given. These values are obtained by running the test computations with the initial data (34) till $t = 100$ and $t = 50$, respectively.

TABLE I: Convergence of the algorithm for solving WKE for the fixed $M = 128$, $t = 100$ and various values of the time step dt

dt	$R_{dt}(n)$	$R_{dt}(K_N)$	$R_{dt}(\Delta_{K_N})$	$R_{dt}(K_E)$	$R_{dt}(\Delta_{K_E})$
2	6.75E-03	1.98E-03	1.03E-03	6.43E-05	9.51E-05
1	1.72E-03	4.99E-04	2.58E-04	1.58E-05	2.33E-05
1/2	4.32E-04	1.25E-04	6.45E-05	3.89E-06	5.75E-06
1/4	1.08E-04	3.12E-05	1.61E-05	9.65E-07	1.43E-06
1/8	2.71E-05	7.80E-06	4.02E-06	2.40E-07	3.55E-07

TABLE II: Convergence of the algorithm for solving WKE for the fixed $dt = 0.25$, $t = 50$ and various values of the number M of the nodes of spatial grids

M	$R_M(n)$	$R_M(K_N)$	$R_M(\Delta_{K_N})$	$R_M(K_E)$	$R_M(\Delta_{K_E})$
32	3.61E-03	8.98E-04	8.37E-04	7.87E-04	3.73E-03
64	1.54E-05	4.37E-06	1.45E-06	7.98E-07	1.01E-05
128	1.85E-10	6.70E-09	1.50E-09	7.49E-11	4.94E-10

We can state from these results that the rate of convergence with respect to time step is close to 2 that strictly corresponds to the theoretical estimates of the error of RK2. The convergence with respect to the number of nodes of the spatial grids is exponential, which also agrees with theoretical predictions and with the data from [6].

The described results are obtained for the times $t = 100$ and $t = 50$ that are rather far from the time $t^* \approx 126.7$, at which the solution of the WKE blows up. For the times close to t^* most of approximations to the solution fail. Let us finalize our research by studying the convergence of the numerical solutions of the WKE and the conservation of the invariants, namely the density of particles and of energy, in the vicinity of t^* .

To perform this study, we expanded the segment $[\omega_{min}, \omega_{max}]$ to $[0.001, 100^2]$, started with initial data (34) and ran the computations with $M = 256$ and with manual adaptation of dt till $t = t_0 \approx 124.14$. The adaptation is done in order to decrease the relative deviations of invariants from their initial values as much as possible. At the point $t = t_0$ the deviations start to grow rapidly, and we use the solution at $t = t_0$ as an initial data for our analysis.

First, we analyse the convergence with respect to the time step by observing the values of $R_{dt}(n)$ for the fixed $M = 256$ at $t \approx 125.7$. From the data in Table III one can see that the impact of the time-stepping error is rather small, and the order of convergence corresponds to theoretical value.

TABLE III: Values of $R_{dt}(n)$ obtained with the fixed $M = 256$ at $t \approx 125.74$

dt	0.16	0.08	0.04	0.02	0.01	0.005
$R_{dt}(n)$	0.0031	8.7E-04	1.9E-04	4.9E-05	1.2E-05	3.1E-06

Second, we consider the convergence of approximations in ω -variable. In Table IV the values of $R_M(n)$ computed for $\omega \in [0.1^2, 86^2]$ are given for different M . The time step is fixed, $dt = 0.08$. In this experiment we are focused on growth of the error in the vicinity of blow up time. Therefore, we observe several time moments close to t^* .

TABLE IV: Values of $R_M(n)$ obtained with the fixed step $dt = 0.08$ at various times close to t^*

M	$t \approx 124.22$	$t \approx 124.7$	$t \approx 125.18$	$t \approx 125.74$
64	0.0199	0.1365	0.2592	0.4343
128	0.0199	0.1316	0.2036	0.2677
256	0.0155	0.1007	0.1982	0.3543
512	0.0046	0.0365	0.0483	0.1458

For the numerical values of spectra obtained in the case $M = 1024$ we compute the relative deviations of the particle and energy densities from their initial values. They are denoted by $D_N(t)$ and $D_H(t)$, respectively, and presented in Table V. The formulas for them are

$$D_N(t) = \frac{N(t) - N(0)}{N(0)}, \quad D_H(t) = \frac{H(t) - H(0)}{H(0)},$$

where $N(t)$ and $H(t)$ are computed by substituting the numerical solution of the WKE obtained for the time moment t into (15), (16).

From the presented results one can conclude that the error of the numerical solution grows rapidly in the vicinity of blow up time, and even the usage of rational approximations with huge number of nodes does not allow us to come very close to t^* . The last more or less adequate approximation of the solution can be obtained at $t \approx 125.7$. The possible reason is that we used rational

TABLE V: Relative deviation of $D_N(t)$ and $D_H(t)$ at various times close to t^* obtained in computations with $M = 1024$, $dt = 0.08$

	$t \approx 124.22$	$t \approx 124.7$	$t \approx 125.18$	125.74
$D_N(t)$	8.69E-05	7.61E-05	3.88E-05	-3.705E-04
$D_H(t)$	-1.86E-04	-1.96E-04	-2.12E-04	-1.87E-04

approximations only for the spectrum, not for the integrands of the collision terms, which obviously also have strong singularities in the vicinity of t^* . Further developments will be directed to design of new cubature formulas aimed at the improvement of this drawback.

An interesting fact is that rather large deviations of the numerical solutions reported in the last column of

Table IV does not affect so much the conservation of invariants. In simulation with $M = 1024$ the value of $|D_N|$ jumps a bit to the order of 10^{-4} , and $|D_H|$ remains practically unchanged. The reason is that the largest deviations of numerical solutions in tests with different M , and hence the errors, are localized in vicinity of the point ω_{min} , whereas in all other points of the domain $[\omega_{min}, \omega_{max}]$ they remain relatively small. For example, comparison of 512 and 1024 results on the segment $[1, \omega_{max}]$ gives the relative deviation less than 10^{-3} .

While comparing the non-conservation of particle and energy densities, one should bring in mind the definitions (15), (16). Due to the factor $\omega^{1/2}$ in (15) the density of particles is more sensitive to the error of spectrum in the vicinity of ω_{min} than the density on energy. That is why for the times close to t^* the deviation $D_N(t)$ starts to grow first.

-
- [1] D. V. Semikoz and I. I. Tkachev, Kinetics of Bose condensation, *Physical review letters* **74**, 3093 (1995).
- [2] R. Lacaze, P. Lallemand, Y. Pomeau, and S. Rica, Dynamical formation of a Bose–Einstein condensate, *Physica D: Nonlinear Phenomena* **152**, 779 (2001).
- [3] C. Connaughton and Y. Pomeau, Kinetic theory and Bose–Einstein condensation, *Comptes Rendus Physique* **5**, 91 (2004).
- [4] N. Bell, V. Grebenev, S. Medvedev, and S. Nazarenko, Self-similar evolution of Alfvén wave turbulence, *Journal of Physics A: Mathematical and Theoretical* **50**, 435501 (2017).
- [5] N. K. Bell and S. V. Nazarenko, Reflected wave solution of Alfvén wave turbulence, *Journal of Physics A: Mathematical and Theoretical* **51**, 405501 (2018).
- [6] B. Semisalov, V. Grebenev, S. Medvedev, and S. Nazarenko, Numerical analysis of a self-similar turbulent flow in Bose–Einstein condensates, *Communications in Nonlinear Science and Numerical Simulation*, 105903 (2021).
- [7] S. Nazarenko, *Wave turbulence*, Vol. 825 (Springer Science & Business Media, 2011).
- [8] Y. V. Lvov and S. Nazarenko, Noisy spectra, long correlations, and intermittency in wave turbulence, *Phys. Rev. E* **69**, 066608 (2004).
- [9] Y. Choi, Y. V. Lvov, and S. Nazarenko, Probability densities and preservation of randomness in wave turbulence, *Physics Letters A* **332**, 230 (2004).
- [10] Y. Choi, Y. V. Lvov, S. Nazarenko, and B. Pokorni, Anomalous probability of large amplitudes in wave turbulence, *Physics Letters A* **339**, 361 (2005).
- [11] Y. Choi, Y. V. Lvov, and S. Nazarenko, Joint statistics of amplitudes and phases in wave turbulence, *Physica D: Nonlinear Phenomena* **201**, 121 (2005).
- [12] V. E. Zakharov, V. S. L’vov, and G. Falkovich, *Kolmogorov spectra of turbulence 1: Wave turbulence*, Springer Series in Nonlinear Dynamics (1992).
- [13] V. Shrira and S. Nazarenko, *Advances In Wave Turbulence*, World Scientific Series On Nonlinear Science Series A (World Scientific Publishing Company, 2013).
- [14] Y. Deng and Z. Hani, Full derivation of the wave kinetic equation, arXiv preprint arXiv:2106.0981 (2021).
- [15] A. Korotkevich, A. Pushkarev, D. Resio, and V. Zakharov, Numerical verification of the weak turbulent model for swell evolution, *European Journal of Mechanics - B/Fluids* **27**, 361 (2008).
- [16] L. Pítajevskij and S. Stringari, *Bose–Einstein Condensation*, International Series of Monographs on Physics (Clarendon Press, 2003).
- [17] S. Dyachenko, A. Newell, A. Pushkarev, and V. Zakharov, Optical turbulence: weak turbulence, condensates and collapsing filaments in the nonlinear Schrödinger equation, *Physica D: Nonlinear Phenomena* **57**, 96 (1992).
- [18] D. V. Semikoz and I. I. Tkachev, Condensation of bosons in the kinetic regime, *Physical review D* **55**, 489 (1997).
- [19] D. Proment, M. Onorato, P. Asinari, and S. Nazarenko, Warm cascade states in a forced-dissipated Boltzmann gas of hard spheres, *Physica D: Nonlinear Phenomena* **241**, 600 (2012).
- [20] Y. Choi, S. Jo, Y.-S. Kwon, and S. Nazarenko, Nonstationary distributions of wave intensities in wave turbulence, *Journal of Physics A: Mathematical and Theoretical* **50**, 355502 (2017).
- [21] G. Krstulovic, *A theoretical description of vortex dynamics in superfluids. Kelvin waves, reconnections and particle-vortex interaction*, Habilitation à diriger des recherches, Université Côte d’Azur (2020).
- [22] S. M. Cox and P. C. Matthews, Exponential time differencing for stiff systems, *Journal of Computational Physics* **176**, 430 (2002).
- [23] V. Shukla and S. Nazarenko, Non-equilibrium Bose–Einstein condensation, arXiv preprint arXiv:2105.07274 (2021).
- [24] C. Connaughton, C. Josserand, A. Picozzi, Y. Pomeau, and S. Rica, Condensation of classical nonlinear waves, *Phys. Rev. Lett.* **95**, 263901 (2005).
- [25] S. Chibbaro, G. Dematteis, C. Josserand, and L. Rondoni, Wave-turbulence theory of four-wave nonlinear interactions, *Phys. Rev. E* **96**, 021101(R) (2017).
- [26] M. Tanaka and N. Yokoyama, Numerical verification of the random-phase-and-amplitude formalism of weak tur-

- bulence, Phys. Rev. E **87**, 062922 (2013).
- [27] M. A. Hossain and M. S. Islam, Generalized composite numerical integration rule over a polygon using Gaussian quadrature, Dhaka University Journal of Science **62**, 25 (2014).
- [28] H. E. Salzer, Lagrangian Interpolation at the Chebyshev Points $x_{n,\nu} = \cos(\nu\pi/n)$, $\nu = O(1)n$; some Unnoted Advantages, The Computer Journal **15**, 156 (1972).
- [29] R. Baltensperger, J. Berrut, and B. Noël, Exponential convergence of a linear rational interpolant between transformed Chebyshev points, Math. Comput. **68**, 1109 (1999).
- [30] T. W. Tee and L. N. Trefethen, A Rational Spectral Collocation Method with Adaptively Transformed Chebyshev Grid Points, SIAM Journal on Scientific Computing **28**, 1798 (2006), <https://doi.org/10.1137/050641296>.
- [31] H. A. Jafari-Varzaneh and S. M. Hosseini, A new map for the Chebyshev pseudospectral solution of differential equations with large gradients, Numerical Algorithms **69**, 95 (2015).
- [32] B. Semisalov and G. Kuzmin, Modification of Fourier Approximation for Solving Boundary Value Problems Having Singularities of Boundary Layer Type (2017) pp. 406–422.
- [33] S. Idimeshev, Rational approximation in initial boundary value problems with fronts (in Russian), Computational technologies **25**, 69 (2020).
- [34] W. M. Gentleman, Implementing Clenshaw–Curtis quadrature, II computing the cosine transformation, Communications of the ACM **15**, 343 (1972).